Structure, Vol. 13, 183–195, February, 2005, ©2005 Elsevier Ltd All rights reserved. DOI 10.1016/j.str.2004.11.014

Conformational Changes of p97 during Nucleotide Hydrolysis Determined by Small-Angle X-Ray Scattering

Jason M. Davies,[1] Hirotsugu Tsuruta,[2] Andrew P. May,[1,3] and William I. Weis[1,*]

[1]Department of Structural Biology and Department of Molecular and Cellular Physiology
Stanford University School of Medicine
299 Campus Drive West
Stanford, California 94305

[2]Stanford Synchrotron Radiation Laboratory
Menlo Park, California 94025

Summary

Valosin-containing protein (VCP)/p97 is an AAA family ATPase that has been implicated in the removal of misfolded proteins from the endoplasmic reticulum and in membrane fusion. p97 forms a homohexamer whose protomers consist of an N-terminal (N) domain responsible for binding to effector proteins, followed by two AAA ATPase domains, D_1 and D_2. Small-angle X-ray scattering (SAXS) measurements of p97 in the presence of AMP-PNP (ATP state), ADP-AlF_x (hydrolysis transition state), ADP, or no nucleotide reveal major changes in the positions of the N domains with respect to the hexameric ring during the ATP hydrolysis cycle. Nucleotide binding and hydrolysis experiments indicate that D_2 inhibits nucleotide exchange by D_1. The data suggest that the conversion of the chemical energy of ATP hydrolysis into mechanical work on substrates involves transmission of conformational changes generated by D_2 through D_1 to move N.

Introduction

Valosin-containing protein (VCP)/p97 is a member of the AAA (ATPases associated with various cellular activities) family of proteins (Neuwald et al., 1999; Confalonieri and Duguet, 1995). The hallmark of this family is the presence of one or two copies of a 230–250 residue AAA domain composed of an α/β subdomain and a helical subdomain. These ATPases typically form oligomeric complexes, and they have been implicated in diverse processes such as organelle biogenesis, assembly of mitochondrial membrane proteins, protein degradation, cell cycle control, and signal transduction (Confalonieri and Duguet, 1995; Patel and Latterich, 1998; Beyer, 1997; Vale, 2000). The mechanisms by which the conversion of chemical energy of ATP hydrolysis into mechanical work is accomplished are poorly understood.

p97 appears to have several roles in the cell, of which the best understood is in ubiquitin/proteasome-mediated protein degradation, in particular endoplasmic reticulum-associated degradation (ERAD) (Jarosch et al., 2003; Wang et al., 2004). In ERAD, misfolded proteins are retro-translocated out of the ER membrane into the cytosol, where they are polyubiquitinated for degradation by the proteasome. p97 has been shown to bind to the ER membrane through interaction with VIMP (Ye et al., 2004). It recognizes and binds substrates both directly and when the substrate is ubiquitinated, through interactions with the Ufd1-Npl4 complex (Meyer et al., 2002), and subsequently extracts the substrate from the membrane. The substrate is then degraded by the 26S proteasome, to which p97 binds (Dai et al., 1998). p97 is also thought to have a role in the reconstitution of the ER and Golgi apparatus following cell division (Kondo et al., 1997; Rabouille et al., 1998). It is possible that p97 facilitates homotypic membrane fusion by virtue of its ability to bind to p47, which in turn binds to the SNARE protein syntaxin 5. The recently identified protein VCIP135 (valosin-containing protein [VCP] p97/p47 complex-interacting protein, p135) can bind to the syntaxin5/p47/p97 complex and promote disassembly through p97-catalyzed ATP hydrolysis (Uchiyama et al., 2002).

Structural studies of p97 and its homologs have yielded few clues as to how energy from ATP hydrolysis is transformed into mechanical work. p97, like most AAA proteins, forms homohexamers (Confalonieri and Duguet, 1995; Peters et al., 1992; Rockel et al., 1999; Hanson et al., 1997; Fleming et al., 1998). The p97 protomer comprises an N-terminal ~200 amino acid domain, designated N, followed by two AAA domains, D_1 and D_2. The N domain interacts with a number of adaptor proteins that are believed to direct the chaperone activity of the enzyme into distinct pathways. Crystal structures of full-length p97 show that the AAA domains form two stacked rings, and the N domains project out from the D_1 ring in a nearly coplanar manner (Zhang et al., 2000; Huyton et al., 2003; DeLaBarre and Brunger, 2003). Cryo-electron microscopic (cryo-EM) reconstructions have provided low-resolution images in four nucleotide states: no nucleotide (NN), bound to the slowly hydrolyzable ATP analog AMP-PNP, bound to the transition state analog ADP-AlF_x, and bound to ADP. While these images show some changes in the D_1 and D_2 rings, the most striking feature is that significant density attributable to the N domain is only seen in the transition state in one study (Rouiller et al., 2002) and in the ATP analog state in another (Beuron et al., 2003). This suggests that the substrate binding N domain is flexibly linked to D_1 in some states and is averaged out in the process of reconstruction.

Here, we present biochemical and small-angle X-ray scattering (SAXS) studies of p97 in four nucleotide states. Models derived from the scattering data reveal significant differences in the position of the N domains, as well as smaller differences in the D_1 and D_2 domains, as the enzyme progresses through the hydrolysis cycle. In contrast to the full-length protein, a fragment lacking the D_2 domain does not undergo significant changes in the position of N, implying that nucleotide hydrolysis by

*Correspondence: bill.weis@stanford.edu

[3]Present address: Fluidigm Co., 7100 Shoreline Court, South San Francisco, California 94080.

D_2 is responsible for conformational changes that link ATPase activity to movement of the N domain.

Results

HPLC Analysis of Nucleotide State

To date, three crystal structures of p97 have been reported, one of the ND_1 fragment and two of the full-length molecule. Regardless of the nucleotide used in crystallization, these structures consistently show ADP bound to D_1, thus leading to the hypothesis that D_1 does not turn over nucleotide (DeLaBarre and Brunger, 2003). On the other hand, biochemical studies have suggested that this domain is active. To assess the nucleotide state in solution near physiological pH and ionic strength, nucleotides were exchanged into ND_1 and full-length p97. The protein was then denatured with urea, and the released nucleotide was analyzed by HPLC. Purified full-length p97 that had been treated with apyrase was found to have no nucleotide bound (Figure 1A). Incubation of purified p97 with excess ADP showed a single peak with the same retention time as an ADP standard. In contrast, protein that had been incubated with the slowly hydrolyzable ATP analog AMP-PNP showed two peaks, corresponding to AMP-PNP and to ADP (Figure 1A); the areas under the AMP-PNP and ADP peaks are about equal, and the total area is approximately equal to that of the single peak in the ADP-treated sample (Figure 1B). Protein that was dialyzed against nucleotide-free buffer ("No Nucleotide") showed a single peak corresponding to ADP, but with only half the integrated area of the ADP-treated sample. These results are consistent with prior structural observations that, in full-length p97, ADP is always bound to D_1 and does not exchange, whereas D_2 actively turns over ATP.

In order to assess whether D_2 inhibits ATP turnover by D_1 in full-length p97, the identity of nucleotides bound to the ND_1 fragment was determined. Samples showed nearly complete exchange with the nucleotide present in solution (Figure 1B). Next, the ATPase activities of wild-type and hydrolysis-impaired ND_1 mutants E305Q and K251A (Wang et al., 2003a) were compared by HPLC analysis. Wild-type and mutant ND_1 proteins were incubated with excess ATP. Magnesium was then added to start the hydrolysis reaction, and aliquots were removed and denatured at 10 s intervals for analysis of bound nucleotide by HPLC. At each time point, two peaks, one corresponding to ATP and the other to ADP, were apparent (data not shown). The ATP peak predominates at early time points, but over 100 s, the ATP peak shrinks and the ADP peak grows, indicating active hydrolysis by the wild-type protein (Figure 1C). In contrast, no activity is detected in the K251A mutant, ruling out the possibility that a contaminating ATPase is producing ADP (Figure 1C). The E305Q mutant displays some activity, but it is approximately half that of the wild-type protein. These data show that the D_1 ATPase is competent for hydrolysis at physiological temperatures, at least in the absence of D_2. Song et al. (2003) and Meyer et al. (1998) reported V_{max} values for hydrolysis by full-length p97 at 37°C of 0.52 nmol min^{-1} μg^{-1} and 0.3 nmol min^{-1} μg^{-1}, respectively, and Song et al. (2003) reported an approximate 10-fold decrease in rate for ND_1 (Meyer et al., 1998; Song et al., 2003). Calculation of the rate from a rough linear fit to the present data gives a value on the order of 20-fold lower than the previously reported values for V_{max} for ND_1.

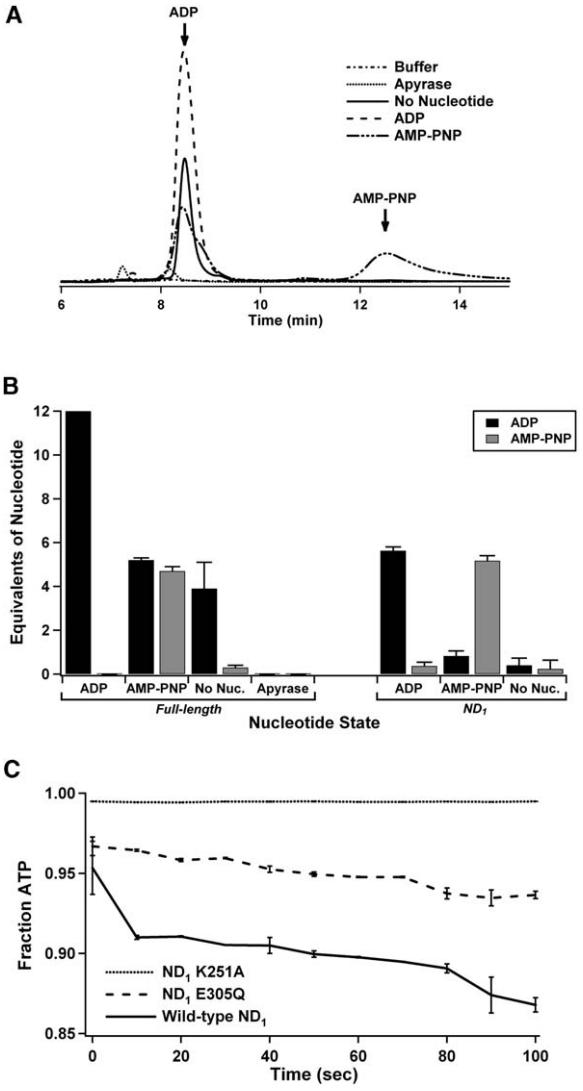

Figure 1. Nucleotide Analyses of Full-Length p97 and ND_1

(A) Representative traces from HPLC analysis of nucleotides bound to full-length p97. Elution times of nucleotide standards ADP and AMP-PNP are indicated by arrows.

(B) Nucleotide analysis of full-length p97 by HPLC. Areas under peaks corresponding to nucleotide standards (black or gray) were normalized across nucleotide state and averaged with runs of like nucleotide state. Labels on the x axis refer to the identity of the exchanged nucleotide. Although efforts were made to standardize protein loading, substoichiometric quantities of nucleotides are likely due to differences in the amount of protein loaded due to the numerous washing steps.

(C) HPLC analysis of hydrolytic activity of wild-type p97 ND_1 and K251A and E305Q mutants at 37°C over the course of 100 s. Proportions of nucleotides present in solution are represented as the fraction of total nucleotide that is in the form of ATP.

Small-Angle Scattering Data

Conformational changes through the course of nucleotide hydrolysis were analyzed in solution by SAXS. Full-

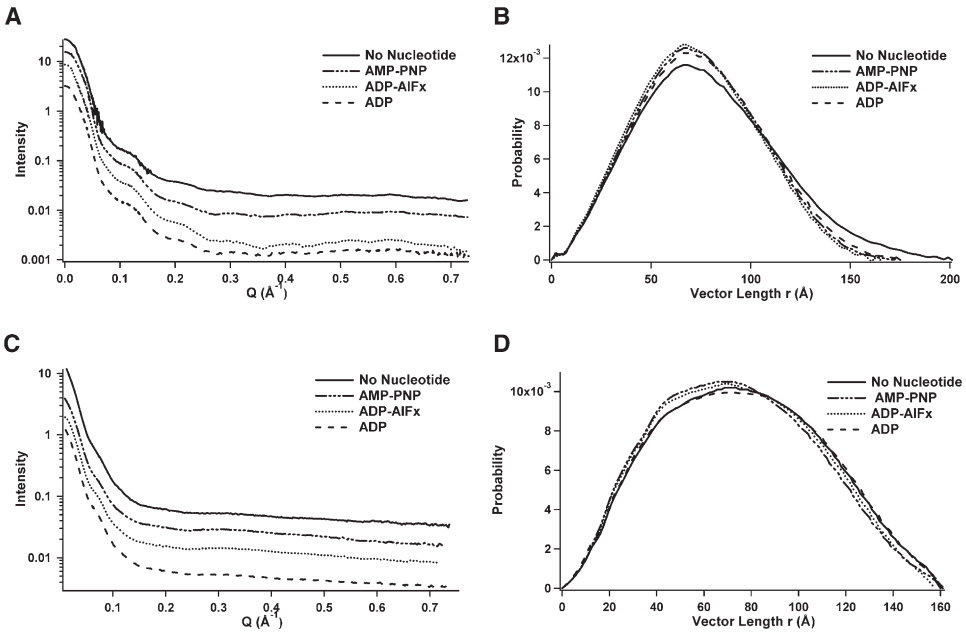

Figure 2. Experimental SAXS Data from Full-Length p97 and ND_1

(A and C) Scaled and spliced X-ray solution scattering data of full-length p97 and ND_1, respectively. Data have been offset along the vertical axis to facilitate visualization.

(B and D) Pair-distance distribution functions as computed from scattering data of full-length p97 and ND_1, respectively.

length p97 was prepared in four states: No Nucleotide, AMP-PNP bound, ADP-AlF_x bound, and ADP bound, where the names refer to the state of D_2. Data were measured to a nominal resolution limit of 8.6 Å. Typical scattering profiles of each state are shown in Figure 2A. The low-angle regime is very similar in each state, whereas more divergence is seen starting at about Q = 0.145 Å^{-1}. A summary of the radius of gyration, R_g, and the maximum interatomic vector length, D_{max}, in each nucleotide state is presented in Table 1. These parameters indicate that in the absence of nucleotide, the complex is in a relatively expanded conformation, exhibiting the largest R_g and D_{max} of the four states. The molecule undergoes significant compaction upon binding of nucleotide, with a 4 Å decrease in R_g and a 26 Å diminution of D_{max}. This is consistent with the 10 Å diminution in the radii of the D_1 and D_2 rings of p97 observed in cryo-EM reconstructions (Rouiller et al., 2002), as well as large changes in tryptophan fluorescence and loss of protease sensitivity upon binding (Wang et al., 2003b). Hydrolysis of the nucleotide to the ADP-P_i state leads to further compaction, and release of P_i to generate the ADP bound state induces a small expansion.

The availability of a crystal structure for full-length p97 bound to ADP-AlF_x (DeLaBarre and Brunger, 2003) allows direct comparison with the SAXS data of this state. The longest interatomic vectors are those that span the molecule from one N domain to another across the hexamer, and from an N domain diagonally across the molecule to the bottom of the D_2 domain on the opposite side. The R_g and D_{max} computed from the crystal structure (PDB ID 1OZ4) are 54.4 Å and 166 Å, respectively. The crystal structure is missing a number

Table 1. X-Ray Scattering Data Statistics

	Full-Length		ND_1 Mutant	
Nucleotide State	R_g	D_{max}	R_g	D_{max}
No Nucleotide	60.6 ± 0.4	201 ± 5	58.9 ± 0.5	160 ± 5
AMP-PNP	56.5 ± 0.2	175 ± 5	56.8 ± 0.3	162 ± 5
ADP + AlF_x[a]	55.4 ± 0.4	165 ± 5	57.3 ± 0.3	158 ± 5
ADP[b]	57.7 ± 0.2	176 ± 5	59.0 ± 0.4	161 ± 5

All values are in Å. R_g values were computed as described in the Experimental Procedures section. The estimated error in R_g for a given value of D_{max} is about ±0.1 Å. Because these two parameters are coupled, the error values for R_g that are shown were obtained by computing R_g over the indicated range of D_{max}. R_g values obtained from the Guinier approximation, which are independent of D_{max}, were very similar (at most 0.2 Å from the indicated value).

[a] R_g and D_{max} from the full-length hexameric crystal structure (PDB ID 1OZ4) are 54.4 and 166 Å, respectively. The N-terminal 26 residues of D_1, residues 586–597, 634–637, 705–731, and the C-terminal 42 residues of D_2 are absent in the structure.

[b] R_g and D_{max} from the hexameric ND_1 fragment crystal structure (PDB ID 1E32) are 54.0 and 166 Å, respectively. The N-terminal 20 residues of N and the C-terminal 2 residues of D_1 are absent in the structure.

of residues, mostly at the C terminus, that could make the computed values of R_g and D_{max} differ from those obtained by SAXS. However, since the D_{max} corresponds to the vector from one N domain across the ring to the opposite, it is highly probable that the missing residues would only affect the computed R_g, and not the D_{max}. Thus, the computed values compare quite favorably to those found for the ADP-AlF$_x$ scattering data.

The real space interatomic distance vector distribution, or *P(r)*, was obtained by indirect Fourier transformation of the scattering data by using the program GNOM (Svergun, 1992) (Figure 2B). The *P(r)* function for all of the states shows a relatively constant shape up to about 80 Å, above which the curves diverge. This suggests that a significant portion of the structure remains invariant over the course of hydrolysis, most likely the structure of the subdomains. Given that the majority of the divergence is seen in the longer vectors, it is likely that those portions of p97 located around the periphery are most affected by changes in nucleotide state. Comparing the *P(r)* data with the crystal structures, it seems reasonable to expect that the D$_1$ and D$_2$ rings remain relatively constant, whereas the N domains, along with the peripheral portions of the D$_2$ domains, undergo the most dramatic rearrangements.

SAXS data were similarly collected and processed for ND$_1$ in the four nucleotide states (Figures 2C and 2D). There are significant variations in R_g (Table 1). However, D_{max} does not differ significantly among the different states and is within error limits of the value calculated from the crystal structure (PDB ID 1E32) (Zhang et al., 2000). The R_g and D_{max} computed from crystal structure are 54.0 Å and 166 Å, respectively. There are 22 residues missing from this structure, but it is unlikely that this limited number alone accounts for the large difference in R_g.

Modeling of Full-Length Scattering Data

The program GASBOR, which uses a simulated annealing procedure to match the scattering computed from a model consisting of one scatterer per amino acid to the experimental data (Svergun et al., 2001), was used to model the SAXS data. A number of independent runs were performed for each nucleotide state. All runs used data to 8.6 Å, and the 6-fold symmetry observed in crystal structures and cryo-EM analyses of p97 was imposed in the modeling. The models were aligned, averaged, and filtered based on occupancy by using DAMAVER (Volkov and Svergun, 2003) to obtain a "most probable" model for each state (Figure 3).

The problem of model generation from SAXS data is fundamentally underdetermined (Volkov and Svergun, 2003), so although the models closely fit the scattering data (e.g., ADP-AlF$_x$ in Figure 4A), it is essential to assess their validity by independent means. The SAXS models can be compared with crystal structures of two of the states. Comparison of the crystal structure of p97 bound to ADP-AlF$_x$ (DeLaBarre and Brunger, 2003) with the corresponding SAXS model reveals a striking concordance (Figure 4B). The N domains are coplanar with the D$_1$ ring, the periphery of the D$_2$ ring flares at the base, and the cavity at the center of the molecule is reproduced in shape and size. A crystal structure of the No Nucleotide state (Huyton et al., 2003) is similar to the corresponding SAXS map in the ND$_1$ region and in reproducing the internal cavity, but there is a clockwise rotation of nearly 20° in the D$_2$ ring (Figure 4C). These crystals were grown in high salt, acid pH conditions, which inhibit the activity of the enzyme (Song et al., 2003). The closer agreement of the SAXS ADP-AlF$_x$ state with the corresponding crystal structure likely reflects the closer match of buffer conditions, since those crystals were grown in a neutral pH, low-ionic strength buffer.

Although a full atomic model of only one of the nucleotide states is available for comparison (the No Nucleotide crystal structure lacks side chains in the D$_2$ domain [Huyton et al., 2003]), it must be emphasized that the biochemical preparation, data collection, and computational analysis of all four states in this study were performed identically except for the identity of the particular nucleotide added. Given the excellent agreement between the SAXS ADP-AlF$_x$ model and the crystal structure, it is reasonable to assume that the models of other nucleotide states are equally reliable and can be compared with confidence. The extraordinarily close fit of the ADP-AlF$_x$ model to the crystal structure allows the individual domains of p97 to be assigned to the SAXS-derived electron density of this state, and by extension based on visual homology, to the other nucleotide states (Figures 3 and 4B). For example, inspection of the AMP-PNP state indicates significant movement of the N and D$_2$ domains relative to the other states. Flexible docking of the full-length crystal structure into the AMP-PNP model by energy minimization of the individual domains (Wriggers and Birmanns, 2001) shows that such a conformation is plausible (Figure 4D). The docking procedure reveals that the main changes associated with nucleotide hydrolysis are a 20° upward rotation of the N domain about the N-D$_1$ linker arm accompanied by a 10° counterclockwise rotation of the D$_2$ domain and a 10 Å outward translation.

The level of heterogeneity amongst the individual GASBOR models for each state is apparent when the most probable electron density map is compared to the total volume enclosed by the superposition of the individual runs (Figure 5). The close congruence of the individual annealing runs in the ADP and ADP-AlF$_x$ states indicates relative homogeneity. A larger volume surrounds the most probable model in the No Nucleotide and AMP-PNP states, although only 2 of the 11 runs constitute the majority of the extra volume in the AMP-PNP state. Thus, the average domain positions are well established in this state. Underdetermination of the modeling procedure seems an unlikely source of heterogeneity, as all data and models were obtained under identical experimental and computational conditions.

It is possible that the No Nucleotide and AMP-PNP states do not obey 6-fold symmetry as well as the other states. If so, imposition of symmetry during modeling could produce the observed increase in heterogeneity. The heterogeneity may also reflect an increased flexibility in these states. The large volume enclosing the superposition of runs in the No Nucleotide state, combined with the model-independent R_g and D_{max} values being large by comparison to the other states, points to

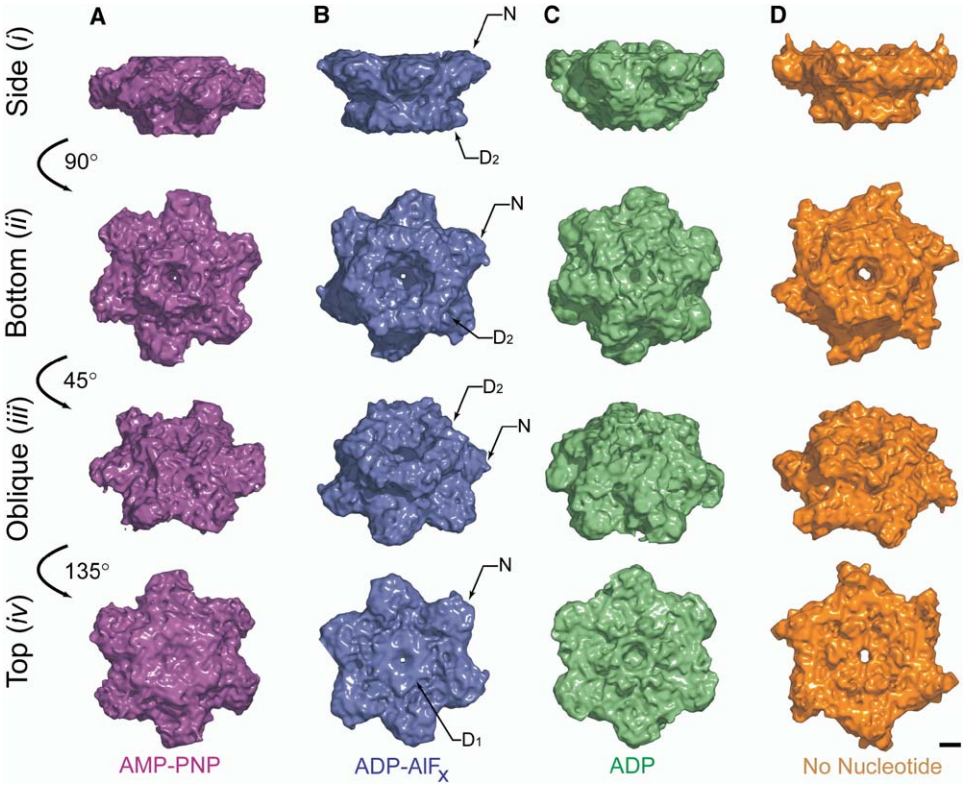

Figure 3. SAXS Models of Full-Length p97

SAXS models of full-length p97 in different nucleotide states: (A) AMP-PNP, (B) ADP-AlF_x, (C) ADP, and (D) No Nucleotide. Each model is represented as an isosurface and viewed from the (row i) side, (row ii) bottom, (row iii) oblique angle, and (row iv) top. Domains are assigned to density in the ADP-AlF_x state, as indicated by the tags N, D_1, and D_2. Scale bar = 20 Å.

a relatively poorly ordered and extended conformation. This is consistent with the increased proteolytic sensitivity of this state (Wang et al., 2003b). Because GASBOR uses a fixed number of constant density scatterers, the location of the density occupied by a flexible portion of the molecule will vary from run to run.

Comparisons of Full-Length p97 in Its Different Nucleotide States

Figure 6 highlights the changes in p97 through its ATP hydrolysis cycle. As expected from the *P(r)* plots, there is a core of each model that remains relatively fixed, consisting primarily of the D_1 and D_2 rings. In the No Nucleotide state, p97 is relatively flat, with the N domains coplanar with the D_1 ring and the base of the D_2 ring flared. The pores of the D_1 and D_2 rings are open, with the pore diameter of D_2 approaching three times that of D_1. As ATP binds, the N domains shift below the plane of the D_1 ring. The D_2 ring rotates approximately 20° clockwise, narrowing its pore by half. As nucleotide is hydrolyzed to the transition state, the N domains once again adopt a coplanar arrangement with respect to D_1. The D_2 pore widens to yield a D_1:D_2 pore ratio of about 1:7, and the ring rotates clockwise an additional 10°. When inorganic phosphate is released from the enzyme, D_2 twists back counter-clockwise about 15°, the periphery again constricts, and the D_2 pore closes to the size of the ATP bound state. In this ADP bound state, smaller yet distinct protrusions reappear at the midline of the molecule. In contrast to the changes in D_2, the D_1 pore size remains relatively constant throughout the cycle, with only a slight expansion in the No Nucleotide state as compared to the other states.

Comparison of the SAXS maps with cryo-EM reconstructions shows some similarities as well as significant differences. The agreement in the ADP-AlF_x state is excellent (data not shown). Rouiller et al. (2002) also reported rotations of D_2 relative to D_1, although the magnitudes are smaller. The increased size of protrusions near the midline between the D_1 and D_2 rings in the ADP bound state seen here, which are likely due to changes in the α-helical subdomain of D_2 (DeLaBarre and Brunger, 2003), are also found in the EM maps of Rouiller et al. (2002). Reconstructions of the ADP and ATP bound states presented by Zhang et al. (2000) and Beuron et al. (2003) have similarity to the SAXS models in the bottom portion of the D_2 ring, with a shape that curves inward as opposed to flaring out as in the ADP-AlF_x state. On the other hand, the sizes of the central pores and their relative changes between states seen here differ from those observed in EM, but it must be noted that these features also differ between the two EM studies.

The most pronounced difference between the SAXS and cryo-EM models is in the location of the N domain.

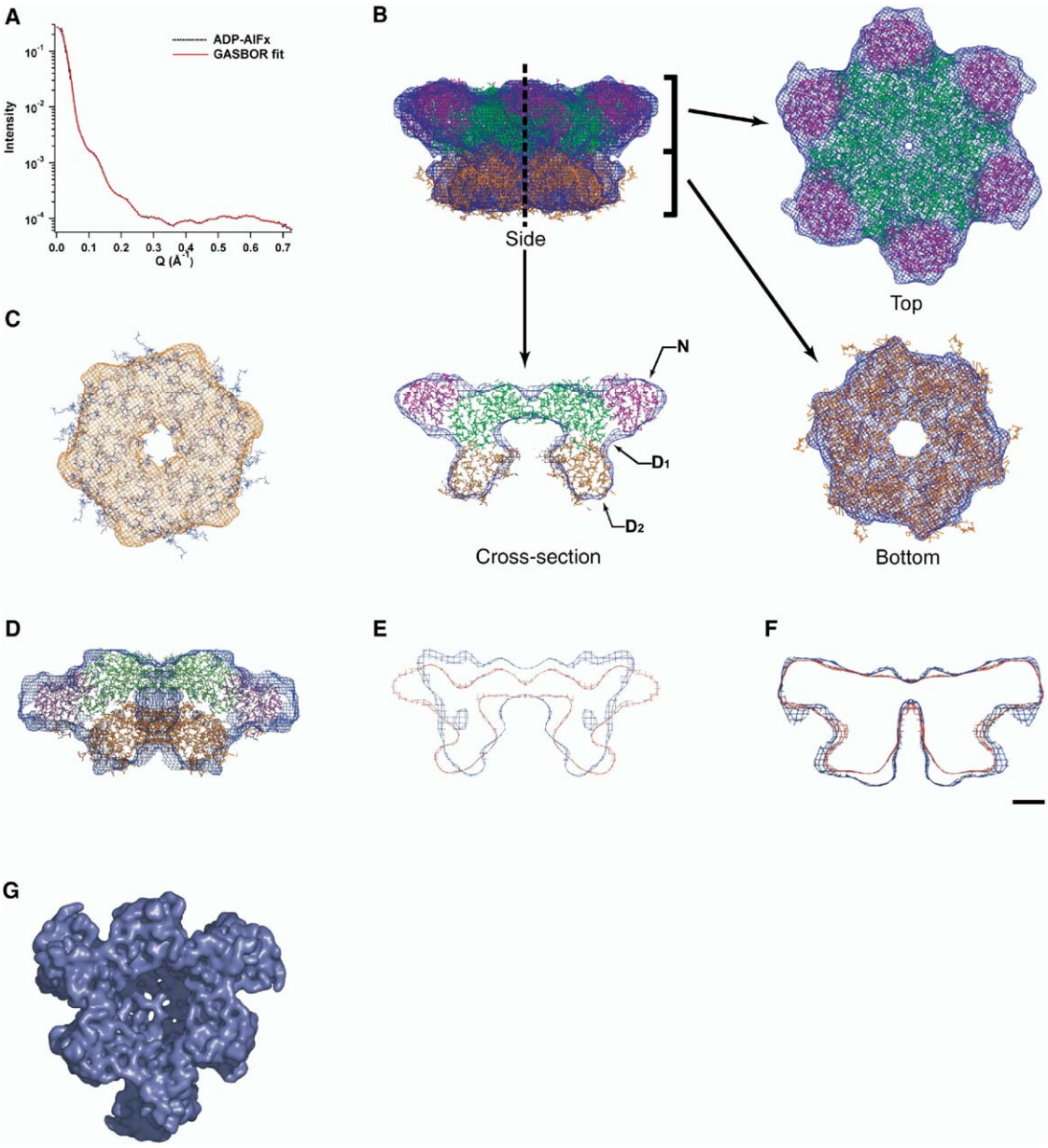

Figure 4. Tests of Model Validity

(A) Comparison of the experimental solution scattering curve (dotted black line) and computed scattering from the ADP-AlF$_x$ model (solid red line).

(B) Full-length SAXS model in the ADP-AlF$_x$ state overlaid on the crystal structure in the same state (PDB ID 1OZ4). The SAXS model is shown as a blue mesh, and the individual domains of the crystal structure are color coded as follows: N = magenta, D_1 = green, D_2 = orange. The upper left panel is a side profile. The lower left panel is a thin vertical slice at the horizontal midline. Domain assignments are indicated by labels N, D_1, and D_2. The upper and lower right panels are top and bottom views, respectively.

(C) Bottom view of the D_2 portion of the SAXS model in No Nucleotide state overlaid on the crystal structure in the same state (PDB ID 1R7R). The SAXS model is shown as an orange mesh, and the D_2 domain of the crystal structure is shown in blue.

(D) Superposition of the full-length crystal structure fit to the SAXS model in the AMP-PNP state shown as thin vertical slices at the horizontal midline.

(E) Comparison of ADP-AlF$_x$ models obtained by using data with different resolution ranges shown as thin vertical slices at the horizontal midline. A representative model based on data with maximum resolution of 8.6 Å in shown in red, and a representative model based on the same data truncated to a maximum resolution of 20.9 Å is shown in blue.

(F) Comparison of models obtained either by using a starting model or ab initio methods shown as thin vertical slices at the horizontal midline. A model of the ADP-AlF$_x$ state consisting of averaged runs obtained by using PDB ID 1OZ4 as the starting structure is shown in red, and an averaged model obtained by using ab initio methods is shown in blue.

(G) Individual GASBOR modeling run of full-length p97 in the presence of ADP-AlF$_x$ with 3-fold symmetry imposed as viewed from the bottom. Scale bar = 20 Å.

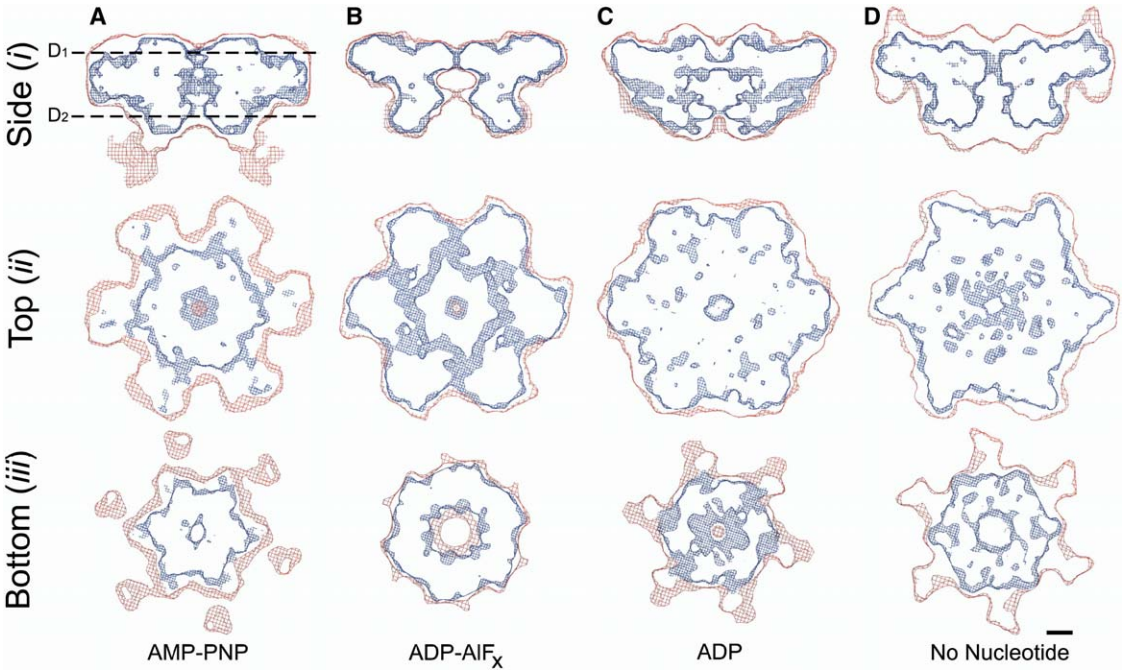

Figure 5. Comparison of Composite and Filtered Models for Full-Length p97

Comparison of composite and filtered models for full-length p97 in four nucleotide states: (A) AMP-PNP, (B) ADP-AlFx, (C) ADP, and (D) No Nucleotide. Aligned, superposed, and summed individual GASBOR runs are shown in red (NN, n = 7; AMP-PNP, n = 11; ADP-AlF$_x$, n = 5; ADP, n = 6), and the final "most probable" model, corresponding to the volume elements of highest occupancy, is shown in blue. Each model is shown as a thin vertical slice at the horizontal midline (row i), as well as horizontal slices at the levels of the (row ii) D_1 and (row iii) D_2 rings, as indicated by the dashed lines in (A), row i. Scale bar = 20 Å.

The SAXS models indicate the location of the N domain in all four nucleotide states. There appears to be some flexibility in the No Nucleotide state, but the N domain was reproducibly found to be coplanar with D_1 in both the ADP-AlF$_x$ and ADP states, and lies below the D_1 plane in the AMP-PNP state. In the study of Rouiller et al. (2002), the N domain could be assigned with confidence only in the ADP-AlF$_x$ state. On the other hand, Beuron et al. (2003) located the N domain in the AMP-PNP bound form, and could ascribe weak density for N in the ADP state. In this AMP-PNP EM reconstruction, the N domain density appears to be partly above the plane of the D_1 ring, in sharp contrast to its position in the SAXS model.

As noted above, there are significant differences between the two EM studies, which complicate comparison with the present SAXS results. Nonetheless, a major difference is that the SAXS data extend to a nominal resolution limit of 8.6 Å, whereas the limits of the EM reconstructions are at 18–24 Å. Truncating the SAXS data to 20.9 Å produces models that differ substantially from those based on higher-resolution data (Figure 4E). These models more closely resemble the EM reconstructions, which is likely due to the absence of the higher-resolution structural information.

Modeling of ND_1 Scattering Data

Modeling of SAXS data obtained from ND_1 was performed identically as above. Ab initio runs or runs from starting models derived from PDB ID 1E32 (Zhang et al., 2000) yielded similar results for each nucleotide state. Figure 7 shows views of the "most probable" model for each nucleotide state. Each of the models has the overall shape of a disk, and all but the No Nucleotide state show clear indication of individual N domains as seen in the crystal structure. Electron density attributable to D_1 can be seen to move appreciably, and it is accompanied by changes in the size and shape of the central pore (Figures 8A–8D), observations consistent with ND_1 being competent for hydrolysis. The N domains are below the plane of the D_1 ring in all states, with minor variations in position (Figure 8E). Superposition of the ADP model of ND_1 with the crystal structure of the same state shows good agreement with the central pore and general shape, but there is significant density below the position of N seen in the crystal structure (Figures 8F and 8G). These data suggest that the solution structure is genuinely different from that seen in crystals. Superposition of the AMP-PNP models for both ND_1 and full-length p97 shows the extent of deflection out of the plane formed by D_1 to be similar and clearly below the position of N as seen in the crystal structure (Figure 8H). The high-salt, acid pH conditions under which the crystals were obtained may be responsible for the differences with the SAXS models.

Discussion

Nucleotide States

The analysis of nucleotides bound to p97 presented here indicates that only half of the nucleotide binding sites can exchange under near-physiological condi-

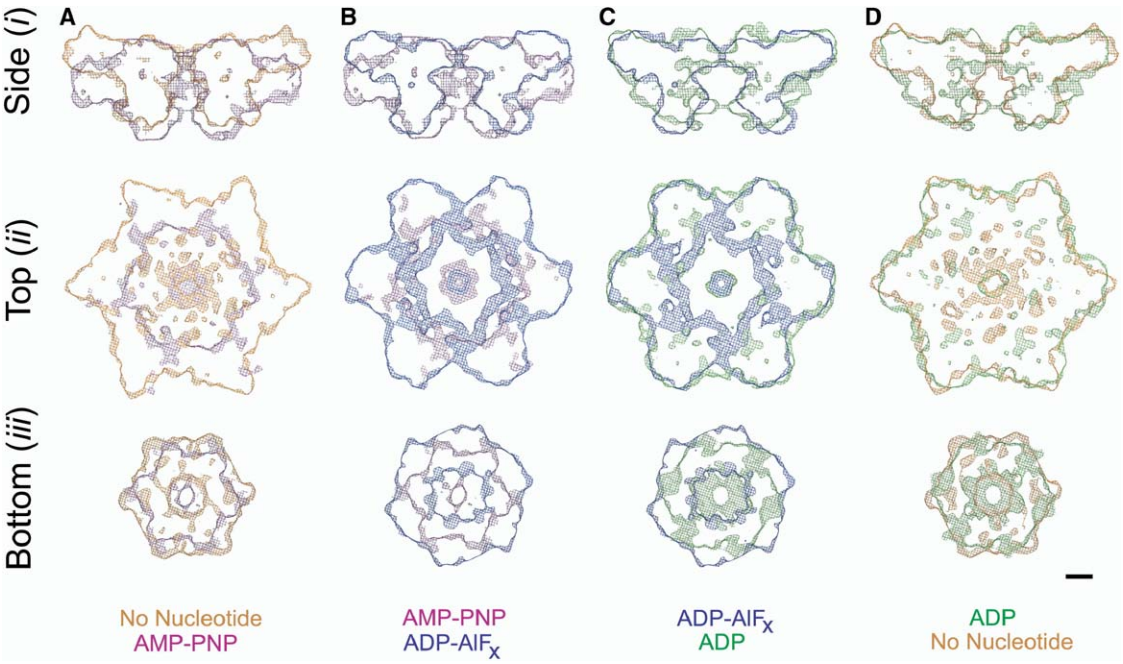

Figure 6. Comparison of Changes Occurring between Nucleotide States in Full-Length p97

Models of all states were rotationally aligned based on a top-down view of ND_1. The colors of each model correspond to those in Figure 3 and are as follows: AMP-PNP = magenta, ADP-AlF$_x$ = blue, ADP = green, No Nucleotide = orange. Each model is shown as a thin vertical slice at (row i) the horizontal midline, as well as horizontal slices at the levels of the (row ii) D_1 and (row iii) D_2 rings. Slices of successive states in the cycle are overlaid to highlight changes as nucleotide (A) binds, is (B) hydrolyzed to transition state, (C) inorganic phosphate is released, and (D) spent nucleotide is released. Scale bar = 20 Å.

tions. These results agree with isothermal titration calorimetry data, which show that only one equivalent of ADP binds per protomer of full-length p97 (DeLaBarre and Brunger, 2003). These data do not rule out the possibility of mixed states in each ring, but when considered with crystallographic observations that ADP is always found in D_1 regardless of the presence or absence of other nucleotides in solution (Zhang et al., 2000; Huyton et al., 2003; DeLaBarre and Brunger, 2003), it appears that D_1 does not readily exchange nucleotide in the context of the full-length protein. Another group has reported that full-length p97 purified in the absence of added nucleotide shows no residual nucleotide, and dialysis of this material suffices to exchange ATP into the enzyme (Wang et al., 2003b). The different results obtained in these studies cannot be readily explained, but may be due to differences in the purification and nucleotide analysis protocols.

In contrast to full-length p97, different nucleotides could be exchanged into ND_1, which was also shown to have ATPase activity. The inability of full-length p97 to exchange nucleotide in D_1 at physiological temperatures suggests that D_2 inhibits the release of ADP bound to D_1. The linker between D_1 and D_2 passes near the nucleotide binding site of D_1 (DeLaBarre and Brunger, 2003) and might block ADP release. Experiments on full-length p97 mutants suggest that the D_1 ring has significant hydrolytic activity at high temperatures (50°–60°C) (Song et al., 2003). Higher temperatures might allow for increased mobility of portions of the polypeptide that block the D_1 binding site, thereby enhancing the hydrolytic activity of this domain. Moreover, binding of adaptor proteins can significantly impact overall ATPase activity in p97 and its homolog NSF (Meyer et al., 1998; Matveeva and Whiteheart, 1998), so conformational changes in the D_1-D_2 linker or elsewhere upon ligand binding may also modulate D_1 activity.

Nucleotide binding by D_1 accelerates, but is not required for, assembly of the p97 hexamer (Wang et al., 2003a). The lack of nucleotide exchange from D_1 suggests that this domain may bind and hydrolyze ATP during the initial assembly of the p97 hexamer, but the resulting ADP is trapped in the D_1 ring. The nucleotide in D_1 may stabilize a particular structure that stimulates D_2. There are changes in overall ATPase activity produced by nucleotide binding (Walker A) or hydrolysis (Walker B) mutations in D_1, which suggested that D_1 is active in full-length p97 (Song et al., 2003; Ye et al., 2003). These data, however, can also be interpreted as indicating that mutations in D_1 produce allosteric changes that diminish the activity of D_2. Indeed, the E305Q hydrolysis mutant of D_1 does not produce significant phenotypic changes in trypanosomes, and produces a phenotype less severe than the equivalent mutation in D_2 in yeast Cdc48p (Ye et al., 2003; Lamb et al., 2001).

Structural analyses of p97 have all been carried out in saturating quantities of nucleotide to ensure sample homogeneity. It is possible that, in vivo, different sub-

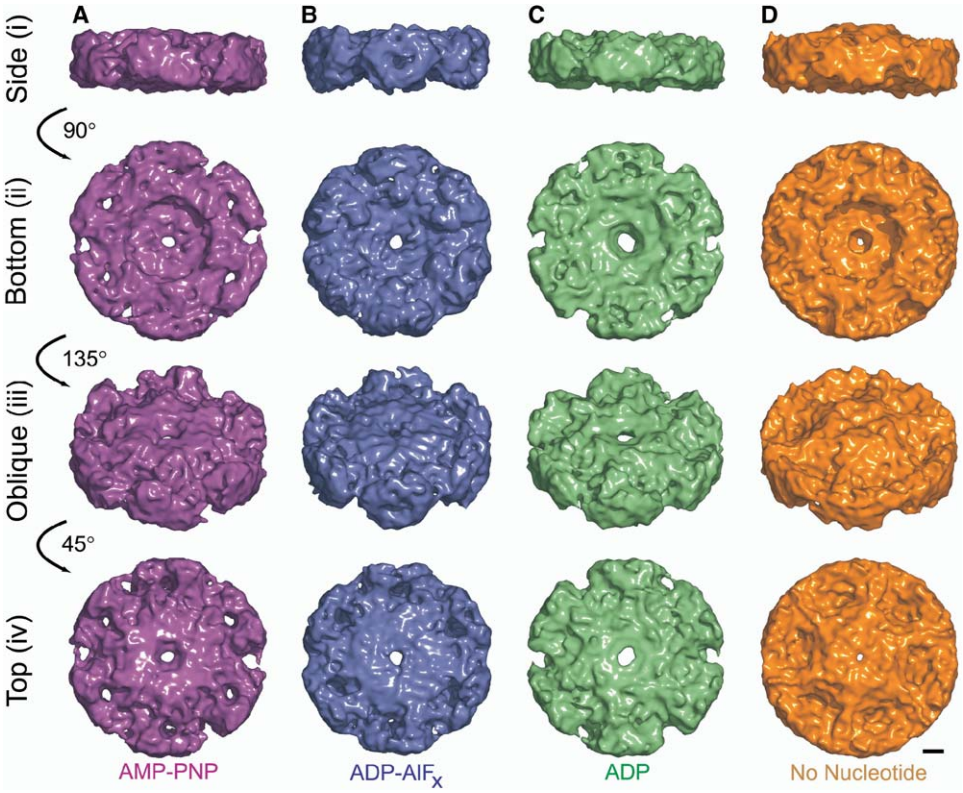

Figure 7. SAXS Models of p97 ND_1

SAXS models of p97 ND_1 in different nucleotide states: (A) AMP-PNP, (B) ADP-AlF_x, (C) ADP, and (D) No Nucleotide. Each model is represented as an isosurface and viewed from the (row i) side, (row ii) bottom, (row iii) oblique angle, and (row iv) top. Scale bar = 20 Å.

units within the hexamer are in different nucleotide states at any given time. Although it is not known if homogeneous nucleotide composition is physiologically accurate, the structural data provide important insights into the range of conformations available to the p97 subunits during the ATPase cycle.

Models and Mechanisms

How does p97 convert the energy of ATP hydrolysis into work done on substrates? The movement of the N domains is likely to be important in transmitting force from the ATPase to substrate or adaptor proteins. The SAXS reconstructions show that, in the ATP bound state, the N domains lie slightly below the D_1 plane, and move up to a position coplanar with D_1 upon hydrolysis (Figure 9). The release of ADP produces a less compact, more flexible structure. Thus, the major changes in N domain positions occur between the No Nucleotide and ATP states, and between the ATP and ADP-AlF_x states, implying that work is done upon binding of ATP, hydrolysis to the ADP-P_i state, or both. In contrast to full-length p97, the N domains of the ND_1 fragment remain below the D_1 plane during its ATPase cycle. The full-length and ND_1 data imply that hydrolysis and release of ATP by D_2 generates the force that moves the N domain, and these data are consistent with the dominant role of D_2 in the activity of p97 (Song et al., 2003). Changes in the central cavity in the vicinity of the D_1-D_2 linker are seen among the nucleotide states (Figure 6), consistent with a role for the linker region in the transmission of force to the N domain (DeLaBarre and Brunger, 2003). The changes in conformation between other states in the cycle may act to reset the system for subsequent rounds. It has been suggested that p97 might feed unfolded substrates into the pore (Ye et al., 2003), and in this regard the alternate opening and closing of the D_2 pore, the relative rotations of the ATPase domains, flaring of the base, and changes in the equatorial protrusions observed through the ATPase cycle may also be important in the activity of the enzyme.

In ERAD extraction of misfolded proteins, p97 is recruited to the ER membrane and anchored through VIMP, whereupon p97 can interact with emerging substrates that are subsequently polyubiquitinated and interact via the Udf1-Npl4 complex. In this case, movements of the N domains could produce a force that pulls the substrate from the membrane. Likewise, in a "pore feeding" mechanism, movements of the N domain could help to feed the substrate into the pore.

p97 shares significant homology with N-ethylmaleimide-sensitive factor (NSF), which mediates disassembly of SNARE complexes after membrane fusion (May et al., 2001). Although NSF disassembles these membrane-anchored complexes, it does not extract the polypeptides from the membrane. This functional difference may be reflected in the organization of the two

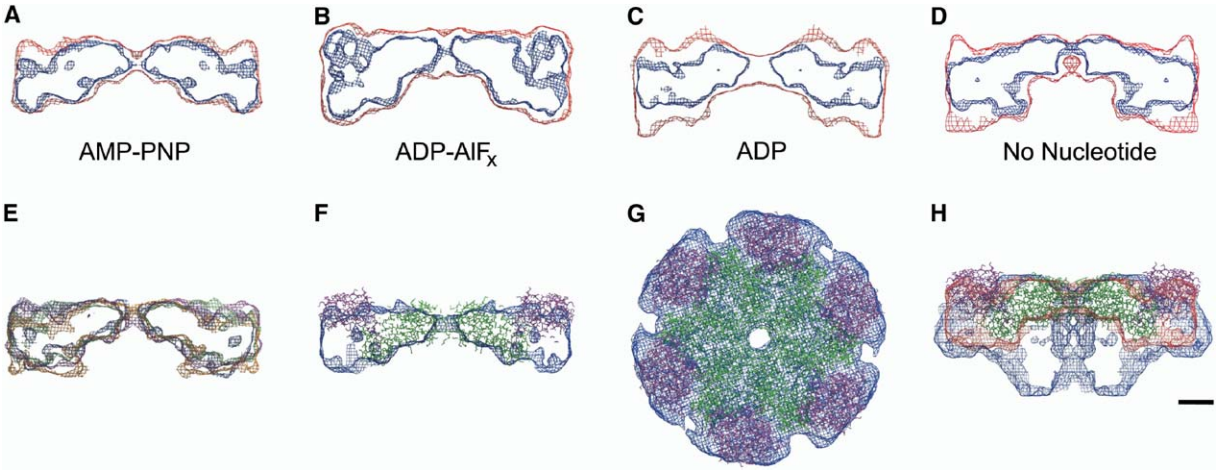

Figure 8. Comparison of Models for p97 ND_1

(A–D) All models are shown as a thin vertical slice at the horizontal midline. Comparison of composite and filtered models in four nucleotide states: (A) AMP-PNP, (B) ADP-AlFx, (C) ADP, and (D) No Nucleotide. Aligned, superposed, and summed individual GASBOR runs are shown in red (NN, n = 6; AMP-PNP, n = 6; ADP-AlF_x, n = 7; ADP, n = 9), and the final "most probable" model, corresponding to the volume elements of highest occupancy, is shown in blue.

(E) Superposition of all hydrolysis states for p97 ND_1. AMP-PNP = magenta, ADP-AlF_x = blue, ADP = green, No Nucleotide = orange.

(F and G) Views of a thin vertical slice at the horizontal midline and top, respectively, of the ND_1 SAXS model in the ADP state overlaid on the crystal structure in the same state (PDB ID 1E32). The SAXS model is shown as a blue mesh, and the individual domains of the crystal structure are color coded as follows: N = magenta, D_1 = green. Note that the asymmetric shape of D_1 leads to an unambiguous fit of the crystal structure to the SAXS model.

(H) Superposition of the AMP-PNP state of full-length (blue mesh) and ND_1(red mesh) with the ND_1 crystal structure (PDB ID 1E32). N = magenta, D_1 = green. Scale bar = 20 Å.

enzymes. In NSF, the D_1 domain is catalytically active, but D_2 has no significant ATPase activity. Therefore, the NSF N domain is linked directly to the ATPase ring responsible for its movements, and this ring presumably undergoes significant conformational changes during its ATPase cycle akin to those seen in p97 D_2. In p97, on the other hand, N is attached to a relatively inactive ring and is moved by forces transmitted from D_2 through or around D_1. The reversed positions of the force-generating ring may reflect different energetic and mechanical requirements for the processes mediated by p97 and NSF. The NSF N domain binds to the SNARE complex through the adaptor α-SNAP, so movements of N such as those documented here for p97 are probably important in the disassembly process. On the other hand, a "pore feeding" model such as that proposed for p97 seems unlikely for NSF, since the SNAREs remain anchored in the membrane.

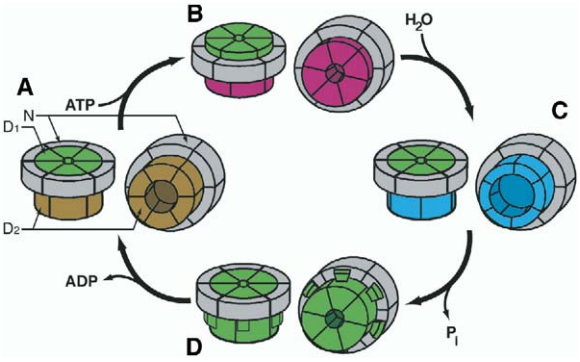

Figure 9. Summary of Major Hydrolysis-Induced Conformational Changes in Full-Length p97

Starting from the (A) No Nucleotide state (shown in oblique side and bottom views), (B) as ATP binds, the N domain shifts below the plane of the D_1 ring, the pore of the D_2 ring narrows by half, and the D_2 ring rotates about 20° clockwise. (C) As nucleotide is hydrolyzed to the transition state, the N domains return to a coplanar arrangement with respect to D_1, the D_2 ring pore widens, and the D_2 ring rotates clockwise an additional 10°. (D) As inorganic phosphate is released from the enzyme, the D_2 ring twists back counterclockwise about 15°, the D_2 pore constricts to the size of the ATP bound state, and protrusions appear at the midline.

The SAXS analysis presented here provides the first view of the p97 N domain position in all four nucleotide states, suggesting how ATP hydrolysis is coupled to conformational changes required for enzyme activity. Powerful modeling algorithms make SAXS a valuable method for examining conformations in solution. Future time-resolved SAXS measurements with rapid mixing devices should allow visualization of conformational changes of p97 in real time.

Experimental Procedures

Protein Purification and Nucleotide Exchange

Full-length p97 (residues 2–806) and the ND_1 truncation mutant (residues 1–460) were expressed with an N-terminal His_6 tag in *E. coli* M15 cells containing the pREP4 plasmid (Qiagen). The protein was purified by successive passage over Ni^{2+}-NTA agarose (Qiagen) and gel filtration (Amersham Biosciences) columns, ending in buffer containing 25 mM Tris (pH 8.5), 300 mM KCl, 5 mM β-mercaptoethanol, 1 mM EDTA, 10% (v/v) glycerol, and 1 mM ATP.

Fractions containing pure p97 were pooled and concentrated by using Vivaspin 20 spin concentrators with a 30,000 Da molecular weight cutoff (Vivascience). The protein was applied to a desalting column (Amersham Biosciences) equilibrated in buffer consisting of 25 mM HEPES (pH 7.1), 150 mM sodium acetate, and 2 mM dithiothreitol, and eluted with the same buffer. The eluate was divided among five tubes, and added to each was 2 mM $MgCl_2$ plus 2 mM or units of one of following enzymes or nucleotides: apyrase, AMP-PNP, ADP, or ADP-AlF_x. The ADP-AlF_x condition was produced by adding 8 mM NaF and 2 mM $AlK(SO_4)_2$ to 2 mM ADP. To the fifth tube, neither nucleotide nor enzyme was added. The protein was concentrated to approximately 20 g/l as estimated by using a dye binding Protein Assay (BioRad). "No Nucleotide" refers to protein to which nothing was added.

HPLC Nucleotide Analysis

In order to identify nucleotides bound to full-length and truncated p97, after exchange, the protein solution was incubated on ice for 30 min and rapidly washed by serial centrifugal filtration steps in a Vivaspin 50,000 Da molecular weight cutoff concentrator (Vivascience), followed by reconstitution with nucleotide-free exchange buffer. This procedure was repeated 2–3 times over a period of 5 min. 400 μg of each sample was denatured in 6 M urea to release bound nucleotide. These solutions, as well as standard solutions of magnesium and nucleotide in 6 M urea, were analyzed on an analytical C18 column with pre-filter (Vydac) on a Hewlett-Packard Ti-Series 1050 HPLC instrument. Nucleotides were eluted isocratically at 1 ml/min in 5 mM tetrabutyl ammonium hydrogen sulfate, 20 mM ammonium phosphate (pH 5.5), and 20% acetonitrile. Elution times and integrated peak areas were determined with the ChemStation software package (Hewlett-Packard).

To assay the ATPase activity of ND_1, the wild-type protein, two hydrolysis mutants, E305Q and K251A, and a buffer blank were nucleotide exchanged as described above and incubated for 1 min on ice with 0.5 mM ATP in the absence of magnesium. The solutions were warmed to 37°C, and 1 mM magnesium chloride was added. Over 100 s, aliquots were removed from each reaction at 10 s intervals, denatured in 6 M urea, and stored on ice pending analysis. Hydrolysis activity was assessed by comparing the ratio of the area under the ATP peak to that of the ADP peak over time after background hydrolysis was taken into account.

Scattering Data Acquisition

Initial SAXS measurements were conducted on beamline 4-2 (Tsuruta et al., 1998) at the Stanford Synchrotron Radiation Laboratory (SSRL), and at beamline 15A (Amemiya et al., 1983) of the Photon Factory (PF). The data reported in this work were measured at the BESSRC-CAT beamline (12-IDC) (Seifert et al., 2000) at the Advanced Photon Source (APS). To avoid aggregation effects in the Guinier region, samples at low concentration (0.5–4 g/l,) were used in conjunction with long detector distances (2–2.8 min, corresponding to an angular range of 0.00407 $Å^{-1} \leq Q \leq = 0.18355\ Å^{-1}$). To improve signal-to-noise at high angles, higher concentrations (10–20 g/l) were used together with short detector distances (0.5–1 min, corresponding to an angular range of $0.02011\ Å^{-1} \leq Q \leq 0.7308\ Å^{-1}$). Data were measured by using a 15 cm × 15 cm nine-element-tiled CCD mosaic detector. The detector channel numbers were converted to momentum transfer $Q = 4\pi\sin(\theta)/\lambda$, where 2θ is the scattering angle and λ is the wavelength (1.30 Å), by using the (100) reflection from a cholesterol myristate powder sample as a standard. The protein and matching buffer solutions were exposed for 5 s, subdivided into five 1 s exposures, in a 1.5 mm quartz capillary flow cell maintained at 15°C. Individual scattering curves were visually inspected prior to averaging to insure that radiation damage was minimal. Scattering from the buffer and cell windows was subtracted after scaling scattering intensities to corresponding incident beam intensities.

Scattering Data Analysis

The raw scattering data were scaled, and buffers were subtracted by using software written by S. Seifert in Igor Pro (Wavemetrics, Inc.). Individual scattering curves for a given state that were collected at different concentrations and over different scattering angle ranges were scaled and merged together in GNOM (Svergun, 1992) to yield a low-noise composite curve covering a wide angular range. The radii of gyration (R_g) were initially computed from the Guinier plot (Guinier and Fournet, 1955). The pair distance distribution function, *P(r)*, was calculated by using the indirect Fourier transform method of Svergun as implemented in GNOM, and values of the R_g were computed from the second moment of the *P(r)* function. These values for R_g compared favorably to the initial values derived from Guinier plots. In order to determine the maximum dimension of the particle (D_{max}), the *P(r)* function was computed while constraining the function to go to zero at r_{max}, where r_{max} was varied from 120 to 210 Å in 1 Å increments. The value of r_{max} that yielded the highest "total estimate" value in combination with a plausible *P(r)* function was taken as the D_{max}.

Modeling of Scattering Data

The program GASBOR (Svergun et al., 2001) was modified by D. Svergun to allow for modeling of molecules in excess of 330 kDa. Each modeling run took 700 hr of CPU time for full-length p97 and 500 hr for ND_1 on a 2.8 GHz Pentium 4 processor. A low-resolution envelope for each state was obtained by superposing individual runs with the program SUPCOMB, which performs an initial alignment of structures using their axes of inertia, followed by minimization of their normalized spatial discrepancy (NSD) (Kozin and Svergun, 2001). The criterion for inclusion in averaging procedures was NSD < mean NSD + 2 * variation. The included aligned structures were averaged by using DAMAVER, giving the equivalent of an occupancy value for each voxel. The models were then filtered based on voxel occupancy with DAMFILT, with the mean volume of the constituent runs set as the cutoff.

GASBOR modeling can be performed either ab initio or from input coordinates. To assess if starting from coordinates biases the resulting GASBOR models, several runs were performed either without a starting model or with the C_α positions from PDB ID 1OZ4. The superposed models agree well both visually (Figure 4F) and computationally, with ab initio models and those starting from coordinates yielding 1.557 ± 0.141 and 1.550 ± 0.114 (NSD ± SD), respectively. This demonstrates that there is no significant bias introduced by the use of starting models, so the final models presented here are averages of both types of simulated annealing protocol.

The effect of symmetry imposition was tested by generating models with 3- or 6-fold symmetry imposed to see if imposition of lower symmetry reproduced the higher-symmetry model. A representative 3-fold model is shown in Figure 4G, which shows rough similarity to the 6-fold models (compare to Figure 3B, row ii). If no symmetry was imposed, the various GASBOR runs showed wide variations in the resulting models (data not shown). These observations suggest that the scattering data do in fact contain 6-fold symmetric information, but also indicate the necessity of imposing the 6-fold symmetry constraint to obtain reliable models.

Flexible docking of the full-length crystal structure (PDB ID 1OZ4) to the AMP-PNP model was performed with SITUS (Wriggers and Birmanns, 2001; Wriggers and Chacon, 2001) by using the monomer, followed by generation of the hexamer by symmetry. For comparison of crystallographic data with models obtained from GASBOR, R_g values and scattering curves were calculated from the crystallographic coordinates by using the program CRYSOL (Svergun et al., 1995). The molecular graphics program Pymol (DeLano, 2002) was used to prepare figures. Angles of domain rotation were measured by fitting the crystal coordinates to the ADP-AlF_x model. The other nucleotide states were aligned to the ND_1 domains, and the D_2 coordinates were rotated to obtain the best visual fit to the map. Changes in pore diameter were measured in the planes shown in Figure 6, rows ii and iii, by using Adobe Illustrator (Adobe Systems Incorporated).

Acknowledgments

We thank S. Seifert and K. Ito for beamline support, B. DeLaBarre for discussions and for providing the ND_1 hydrolysis mutants, D. Svergun for modifying GASBOR for large molecules, and S. Doni-

ach for comments on the manuscript. Portions of this research were carried out at the Photon Factory, the Advanced Photon Source, and the Stanford Synchrotron Radiation Laboratory (SSRL). SSRL is a national user facility operated by Stanford University on behalf of the U.S. Department of Energy (DOE), Office of Basic Energy Sciences. The SSRL Structural Molecular Biology Program is supported by the DOE Office of Biological and Environmental Research, by the National Institutes of Health, the National Center for Research Resources, the Biomedical Technology Program, and the National Institute of General Medical Sciences. Use of the Advanced Photon Source was supported by the DOE Office of Science, Office of Basic Energy Sciences, under Contract No. W-31-109-ENG-38. J.M.D. was supported by the Stanford Medical Scientist Training Program. This work was supported by grant MH58570 to W.I.W. from the National Institutes of Health.

Received: October 6, 2004
Revised: November 15, 2004
Accepted: November 22, 2004
Published: February 8, 2005

References

Amemiya, Y., Wakabayashi, K., Hamanaka, T., Wakabayashi, T., and Hashizume, H. (1983). Design of a small-angle diffractometer using synchrotron radiation at the photon factory. Nucleic Instrum. Methods *208*, 471–477.

Beuron, F., Flynn, T.C., Ma, J., Kondo, H., Zhang, X., and Freemont, P.S. (2003). Motions and negative cooperativity between p97 domains revealed by cryo-electron microscopy and quantised elastic deformational model. J. Mol. Biol. *327*, 619–629.

Beyer, A. (1997). Sequence analysis of the AAA protein family. Protein Sci. *6*, 2043–2058.

Confalonieri, F., and Duguet, M. (1995). A 200-amino acid ATPase module in search of a basic function. Bioessays *17*, 639–650.

Dai, R.M., Chen, E., Longo, D.L., Gorbea, C.M., and Li, C.C. (1998). Involvement of valosin-containing protein, an ATPase co-purified with IkappaBalpha and 26 S proteasome, in ubiquitin-proteasome-mediated degradation of IkappaBalpha. J. Biol. Chem. *273*, 3562–3573.

DeLaBarre, B., and Brunger, A.T. (2003). Complete structure of p97/valosin-containing protein reveals communication between nucleotide domains. Nat. Struct. Biol. *10*, 856–863.

DeLano, W.L. (2002). The PyMOL Molecular Graphics System (San Carlos, CA: DeLano Scientific).

Fleming, K.G., Hohl, T.M., Yu, R.C., Müller, S.A., Wolpensinger, B., Engel, A., Engelhardt, H., Brünger, A.T., Söllner, T.H., and Hanson, P.I. (1998). A revised model for the oligomeric state of the N-ethylmaleimide-sensitive fusion protein, NSF. J. Biol. Chem. *273*, 15675–15681.

Guinier, A., and Fournet, G. (1955). Small Angle Scattering of X-Rays (New York: John Wiley and Sons).

Hanson, P.I., Roth, R., Morisaki, H., Jahn, R., and Heuser, J.E. (1997). Structure and conformational changes in NSF and its membrane receptor complexes visualized by quick-freeze/deep-etch electron microscopy. Cell *90*, 523–535.

Huyton, T., Pye, V.E., Briggs, L.C., Flynn, T.C., Beuron, F., Kondo, H., Ma, J., Zhang, X., and Freemont, P.S. (2003). The crystal structure of murine p97/VCP at 3.6 Å. J. Struct. Biol. *144*, 337–348.

Jarosch, E., Lenk, U., and Sommer, T. (2003). Endoplasmic reticulum-associated protein degradation. Int. Rev. Cytol. *223*, 39–81.

Kondo, H., Rabouille, C., Newman, R., Levine, T.P., Pappin, D., Freemont, P., and Warren, G. (1997). p47 is a cofactor for p97-mediated membrane fusion. Nature *388*, 75–78.

Kozin, M.B., and Svergun, D.I. (2001). Automated matching of high- and low-resolution structural models. J. Appl. Crystallogr. *34*, 33–41.

Lamb, J.R., Fu, V., Wirtz, E., and Bangs, J.D. (2001). Functional analysis of the trypanosomal AAA protein TbVCP with trans-dominant ATP hydrolysis mutants. J. Biol. Chem. *276*, 21512–21520.

Matveeva, E., and Whiteheart, S.W. (1998). The effects of SNAP/SNARE complexes on the ATPase of NSF. FEBS Lett. *435*, 211–214.

May, A.P., Whiteheart, S.W., and Weis, W.I. (2001). Unraveling the mechanism of the vesicle transport ATPase NSF, the N-ethylmaleimide-sensitive factor. J. Biol. Chem. *276*, 21991–21994.

Meyer, H.H., Kondo, H., and Warren, G. (1998). The p47 co-factor regulates the ATPase activity of the membrane fusion protein, p97. FEBS Lett. *437*, 255–257.

Meyer, H.H., Wang, Y., and Warren, G. (2002). Direct binding of ubiquitin conjugates by the mammalian p97 adaptor complexes, p47 and Ufd1-Npl4. EMBO J. *21*, 5645–5652.

Neuwald, A.F., Aravind, L., Spouge, J.L., and Koonin, E.V. (1999). AAA^{+}: a class of chaperone-like ATPases associated with the assembly, operation, and disassembly of protein complexes. Genome Res. *9*, 27–43.

Patel, S., and Latterich, M. (1998). The AAA team: related ATPases with diverse functions. Trends Cell Biol. *8*, 65–71.

Peters, J.-M., Harris, J.R., Lustig, A., Müller, S., Engel, A., Volker, S., and Franke, W.W. (1992). Ubiquitous soluble Mg^{2+}-ATPase complex: a structural study. J. Mol. Biol. *223*, 557–571.

Rabouille, C., Kondo, H., Newman, R., Hui, N., Freemont, P., and Warren, G. (1998). Syntaxin 5 is a common component of the NSF- and p97-mediated reassembly pathways of Golgi cisternae from mitotic Golgi fragments in vitro. Cell *92*, 603–610.

Rockel, B., Walz, J., Hegerl, R., Peters, J., Typke, D., and Baumeister, W. (1999). Structure of VAT, a CDC48/p97 ATPase homologue from the archeon *Thermoplasma acidophilum* as studied by electron tomography. FEBS Lett. *451*, 27–32.

Rouiller, I., DeLaBarre, B., May, A.P., Weis, W.I., Brunger, A.T., Milligan, R.A., and Wilson-Kubalek, E.M. (2002). Conformational changes of the multifunction p97 AAA ATPase during its ATPase cycle. Nat. Struct. Biol. *9*, 950–957.

Seifert, S., Winans, R.E., Tiede, D.M., and Thiagarajan, P. (2000). Design and performance of a ASAXS instrument at the Advanced Photon Source. J. Appl. Crystallogr. *33*, 782–784.

Song, C., Wang, Q., and Li, C.C. (2003). ATPase activity of p97-valosin-containing protein (VCP). D2 mediates the major enzyme activity, and D1 contributes to the heat-induced activity. J. Biol. Chem. *278*, 3648–3655.

Svergun, D.I. (1992). Determination of the regularization parameter in indirect-transform methods using perceptual criteria. J. Appl. Crystallogr. *25*, 498–503.

Svergun, D., Barberato, C., and Koch, M.H.J. (1995). CRYSOL: a program to evaluate x-ray solution scattering of biological macromolecules from atomic coordinates. J. Appl. Crystallogr. *28*, 768–773.

Svergun, D.I., Petoukhov, M.V., and Koch, M.H. (2001). Determination of domain structure of proteins from X-ray solution scattering. Biophys. J. *80*, 2946–2953.

Tsuruta, H., Brennan, S., Rek, Z.U., Irving, T.C., Tompkins, W.H., and Hodgson, K.O. (1998). A Wide-bandpass multilayer monochromator for biological small-angle scattering and fiber diffraction studies. J. Appl. Crystallogr. *31*, 672–682.

Uchiyama, K., Jokitalo, E., Kano, F., Murata, M., Zhang, X., Canas, B., Newman, R., Rabouille, C., Pappin, D., Freemont, P., and Kondo, H. (2002). VCIP135, a novel essential factor for p97/p47-mediated membrane fusion, is required for Golgi and ER assembly in vivo. J. Cell Biol. *159*, 855–866.

Vale, R.D. (2000). AAA proteins. Lords of the ring. J. Cell Biol. *150*, F13–F19.

Volkov, V.V., and Svergun, D.I. (2003). Uniqueness of ab initio shape determination in small-angle scattering. J. Appl. Crystallogr. *36*, 860–864.

Wang, Q., Song, C., and Li, C.C. (2003a). Hexamerization of p97-VCP is promoted by ATP binding to the D1 domain and required for ATPase and biological activities. Biochem. Biophys. Res. Commun. *300*, 253–260.

Wang, Q., Song, C., Yang, X., and Li, C.C. (2003b). D1 ring is stable and nucleotide-independent, whereas D2 ring undergoes major

conformational changes during the ATPase cycle of p97-VCP. J. Biol. Chem. *278*, 32784–32793.

Wang, Q., Song, C., and Li, C.C. (2004). Molecular perspectives on p97-VCP: progress in understanding its structure and diverse biological functions. J. Struct. Biol. *146*, 44–57.

Wriggers, W., and Birmanns, S. (2001). Using situs for flexible and rigid-body fitting of multiresolution single-molecule data. J. Struct. Biol. *133*, 193–202.

Wriggers, W., and Chacon, P. (2001). Modeling tricks and fitting techniques for multiresolution structures. Structure (Camb.) *9*, 779–788.

Ye, Y., Meyer, H., and Rapoport, T.A. (2003). Function of the p97–Ufd1–Npl4 complex in retrotranslocation from the ER to the cytosol: dual recognition of nonubiquitinated polypeptide segments and polyubiquitin chains. J. Cell Biol. *162*, 71–84.

Ye, Y., Shibata, Y., Yun, C., Ron, D., and Rapoport, T.A. (2004). A membrane protein complex mediates retro-translocation from the ER lumen into the cytosol. Nature *429*, 841–847.

Zhang, X., Shaw, A., Bates, P.A., Newman, R.H., Gowen, B., Orlova, E., Gorman, M.A., Kondo, H., Dokurno, P., Lally, J., et al. (2000). Structure of the AAA ATPase p97. Mol. Cell *6*, 1473–1484.